Electronic and transport properties in Ruddlesden-Popper neodymium nickelates $Nd_{n+1}Ni_nO_{3n+1}$ ($n = 1$–5)

Wenjie Sun [1,2] Yueying Li [1,2] Xiangbin Cai [3] Jiangfeng Yang,[1,2] Wei Guo,[1,2] Zhengbin Gu,[1,2] Ye Zhu [4,*] and Yuefeng Nie [1,2,†]

[1]*National Laboratory of Solid State Microstructures, Jiangsu Key Laboratory of Artificial Functional Materials, College of Engineering and Applied Sciences, Nanjing University, Nanjing 210093, China*
[2]*Collaborative Innovation Center of Advanced Microstructures, Nanjing University, Nanjing 210093, China*
[3]*Department of Physics, The Hong Kong University of Science and Technology, Hong Kong, China*
[4]*Department of Applied Physics, Research Institute for Smart Energy, The Hong Kong Polytechnic University, Hong Kong, China*

A series of Ruddlesden-Popper nickelates $Nd_{n+1}Ni_nO_{3n+1}$ ($n = 1$–5) have been stabilized in thin film form using reactive molecular-beam epitaxy. X-ray diffraction and scanning transmission electron microscopy measurements suggest high crystalline quality of these films. The average Ni valence states in these compounds are in accordance with the nominal values, as verified by x-ray photoelectron spectroscopy. The metal-insulator transition temperature (T_{MI}) shows a clear n dependence for $n = 3$–5 members. At low temperature, the resistivity for $n = 3$–5 members exhibits a log T dependence, which is like that reported in parent compounds of superconducting infinite-layer nickelates.

I. INTRODUCTION

Layered nickelates with the chemical formula $R_{n+1}Ni_nO_{3n+1}$ (R = trivalent rare-earth elements), which structurally belong to Ruddlesden-Popper (RP) series [1], have long been considered as promising candidates for realizing high-temperature (high-T_c) superconductivity [2,3]. Indeed, some key features have been revealed in such compounds utilizing angle-resolved photoemission spectroscopy and x-ray absorption spectroscopy, such as the pseudogap in $Nd_{2-x}Sr_xNiO_4$ [4], the large hole Fermi surface with $d_{x^2-y^2}$ character in $La_4Ni_3O_{10}$ [5], and the large orbital polarization in metallic $Pr_4Ni_3O_8$ [6]. More recently, superconductivity has been discovered in hole-doped infinite-layer $NdNiO_2$ [7–9] (the $n = \infty$ member of the reduced RP series), and later in $PrNiO_2$ [10] and $LaNiO_2$ [11,12], which has further triggered intensive research interest in this field. Moreover, the required Ni $3d$ orbital occupancy (or doping level) within the superconducting dome of hole-doped $NdNiO_2$ [8,9] could be achieved by directly reducing RP phases with higher n values ($n = 4, 5$) without any cation substitution [6,13–15]. Thus, it may be possible to realize superconductivity in such compounds and potentially higher T_c given enhanced superexchange interactions, as already observed [16,17]. Also, perovskite nickelates (the $n = \infty$ member of the RP series) possess varieties of exotic properties, among which the metal-insulator transition (MIT) has attracted much attention [18–21], considering its value in both theoretical and experimental sides. It is widely believed that the MIT in nickelates is mainly related to the Ni-O-Ni bond angle [18,22] and can be modulated by structural engineering, such as changing the R size [23] or epitaxial strain [24]. As such, the MIT would be also modulated in the RP series since the insertion of an extra RO layer into the perovskite framework along the c axis causes symmetry breaking in such phases. From these perspectives, RP nickelates with high n values ($3 < n < \infty$) provide a platform for in-depth study of nickelate physics. However, they can only be obtained via layer-by-layer engineering [13], owing to thermodynamic instability. Consequently, the investigation of their physical properties is still lacking.

In this paper, we report the epitaxial stabilization of $Nd_{n+1}Ni_nO_{3n+1}$ ($n = 1$–5) thin films on (001) $LaAlO_3$ (LAO) substrates by reactive molecular-beam epitaxy (MBE). High crystalline quality is confirmed by the combination of high-resolution x-ray diffraction (XRD), atomic force microscopy (AFM), and scanning transmission electron microscopy (STEM). Transport measurements reveal the modulation of MIT by changing the n value, and the valence states of Ni across the RP series are investigated by x-ray photoelectron spectroscopy (XPS).

II. EXPERIMENTAL SECTION

A series of Nd-based RP films were grown on (001)-oriented LAO single-crystal substrates by MBE using a DCA R450 system, and the growth process was monitored by an *in situ* reflection high-energy electron diffraction (RHEED) system. An AlO_2-teminated atomically flat surface of LAO was obtained by the standard etching technique [25]. During the growth, the substrate temperature was fixed at 600 °C (except for the $n = 1$ member at 750 °C), and the background pressure
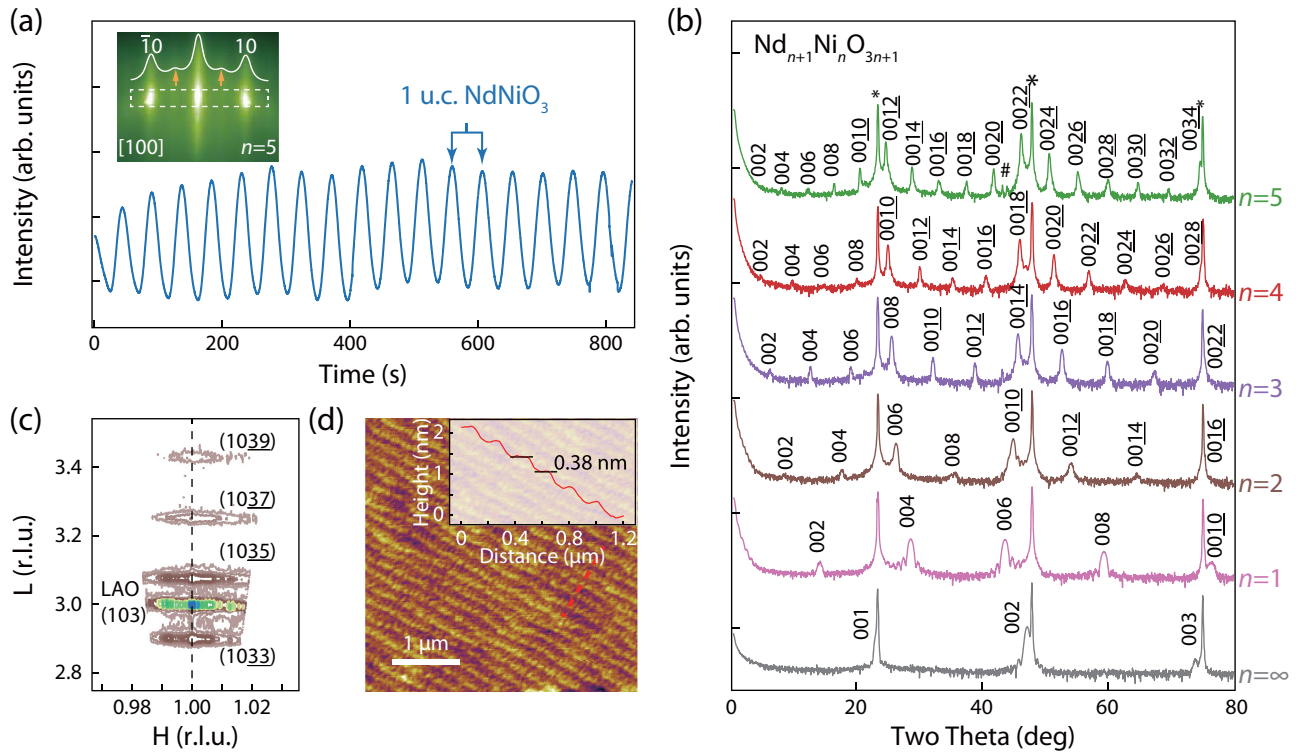
*yezhu@polyu.edu.hk
†ynie@nju.edu.cn

184518-1

FIG. 1. (a) Reflection high-energy electron diffraction (RHEED) intensity oscillations during the codeposition growth of $NdNiO_3$ films. Inset shows the RHEED pattern of the $Nd_6Ni_5O_{16}$ film taken along the [100] pseudocubic direction. White solid line represents the intensity profile integrated along the vertical axis of the rectangular region marked with white dashed line. The half-order peaks caused by oxygen octahedral rotations were indicated by yellow arrows. (b) 2θ-ω x-ray diffraction (XRD) scans of 9-u.c.-thick $Nd_{n+1}Ni_nO_{3n+1}$ Ruddlesden-Popper (RP) films with $n = 1$–5 and 20-u.c.-thick $NdNiO_3$ film (the $n = \infty$ member of RP phases). Diffraction peaks of $LaAlO_3$ (LAO) substrate are denoted by asterisks. All plots are vertically offset for clarity. The peaks marked by # are background diffractions appearing occasionally depending on the exact configuration of the instrument. (c) Reciprocal space mapping (RSM) image of the 9-u.c.-thick $Nd_6Ni_5O_{16}$ around LAO (103). (d) Atomic force microscopy (AFM) image of the 9-u.c.-thick $Nd_6Ni_5O_{16}$ and corresponding line cut (inset) along the red dashed line. The root-mean-square roughness is 94 pm.

was kept $\sim 1 \times 10^{-5}$ Torr of distilled ozone. Such high oxidant partial pressure was utilized to minimize the formation of oxygen vacancy, as reported for growing stoichiometric $LaNiO_3$ [26]. All RP films were obtained by a shuttered layer-by-layer deposition, with the deposition sequence suggested in previous work [27,28]. The deposition time of NdO or NiO_2 monolayer has been precisely calibrated and corresponds to a single period of RHEED intensity oscillation [Fig. 1(a)] in the growth of $NdNiO_3$ $NdNiO_3$ using the codeposition method [29]. It should be noted that the slight overall intensity drift is caused by the background pressure oscillations rather than the wrong dosage of individual sources, which is frequently seen in $SrTiO_3$ growth [29]. All films were grown on the same day to minimize the possible variation in beam fluxes, background pressure, etc. The inset in Fig. 1(a) shows the RHEED pattern of $Nd_6Ni_5O_{16}$ (the $n = 5$ member of the RP series) using the shuttered growth method, and the sharp and bright diffraction spots indicate its high surface crystallinity.

The crystallinity of the RP film was examined by XRD using a Bruker D8 Discover diffractometer. The surface morphology was checked by an Asylum Research MFP-3D system. Samples for cross-sectional STEM measurements were prepared by focused ion beam techniques. Atomic-resolution annular dark-field (ADF) images and energy-dispersive x-

ray spectroscopy (EDX) maps were acquired on the JEOL JEM-ARM200F outfitted with an ASCOR fifth-order probe corrector. The XPS spectra were collected at room temperature with a Thermo Scientific K-Alpha instrument using Al Kα radiation ($h\nu = 1486.6$ eV), with the polar angle of 60°. The pass energy and step size are set at 50 and 0.1 eV, respectively. The flood gun was used during all experiments to prevent possible charging effect, and the main peak position of C 1s (284.8 eV) is used for minor binding energy calibration for all measured spectra. The electrical transport properties were measured using a standard collinear four-point probe method in a homemade closed-cycle cryostat. We also tried to characterize the magnetic properties of RP films (not shown) using a Quantum Design magnetic property measurement system (MPMS3). However, no clear conclusions concerning the magnetic properties can be drawn due to the strong diamagnetic background from LAO substrates.

III. RESULTS AND DISCUSSION

A. Structural characterizations

As shown in Fig. 1(b), sharp diffraction peaks in 2θ-ω scans suggest a single phase of the present RP series. Also, there is no obvious peak splitting, implying the right periodic
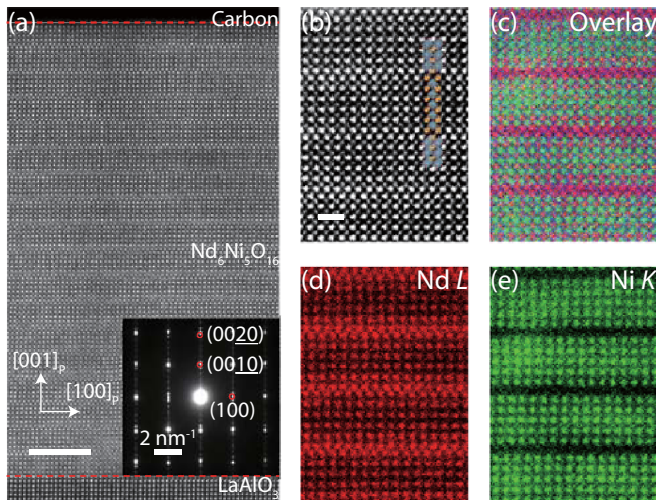
FIG. 2. (a) Cross-sectional annular dark-field (ADF) scanning transmission electron microscopy (STEM) image of a 9-u.c.-thick $Nd_6Ni_5O_{16}$ ($n = 5$) film and the corresponding electron diffraction pattern shown in the inset. The subscript p denotes the pseudocubic notation. Scale bar, 5 nm. (b) Enlarged view of the ADF-STEM image shown in (a) with the crystal structure model overlaid. Scale bar, 1 nm. (c)–(e) Atomic-resolution energy-dispersive x-ray spectroscopy (EDX) maps of Nd + Ni, Nd, and Ni acquired from the same area as (b).

sequence during growth since the minor deviation (1%) of monolayer dosage will lead to peak splitting and shift in RP films [30]. Reciprocal space mapping (RSM) indicates RP films are fully constrained to the substrate, with a representative $n = 5$ member shown in Fig. 1(c). The out-of-plane lattice constants calculated from corresponding RSM results are 12.43 ± 0.01, 20.17 ± 0.02, 27.76 ± 0.01, 35.52 ± 0.02, 43.14 ± 0.01, and 3.85 ± 0.01 Å for the $n = 1$–5 and ∞ phases, respectively. Figure 1(d) shows the AFM topography of the $n = 5$ film in which the smooth surface with step height of ∼0.38 nm (as shown in the inset) reflects the layer-by-layer growth mode, as expected.

It has been documented that some unexpected defects, such as intergrowth [30] and the SrO double-layer missing [27], will appear during the growth of the $Sr_{n+1}Ti_nO_{3n+1}$ RP series. Such defects will prohibit the identification of intrinsic properties, for example, dielectric properties [31,32]. As such, atomic-resolution STEM was performed for the $n = 5$ film to examine the local nanostructures. As shown in Fig. 2(a), the ADF-STEM image and the corresponding electron diffraction pattern reveal the layered structure consisting of alternatively stacked perovskite units and NdO-NdO rock-salt double layers, as expected. Moreover, sharp interfaces with no obvious ionic intermixing can be verified through atomic-resolution EDX maps [Figs. 2(c)–2(e)]. All prove the feasibility of the nonstoichiometric deposition method [27] in growing RP nickelates with high n value at the atomic level.

B. Nickel valence states in RP neodymium nickelates

A prominent feature of layered nickelates is the ability to engineer 3d orbital occupancy of Ni between 3d^8 (divalent for $n = 1$) and 3d^7 (trivalent for $n = \infty$) without chemical
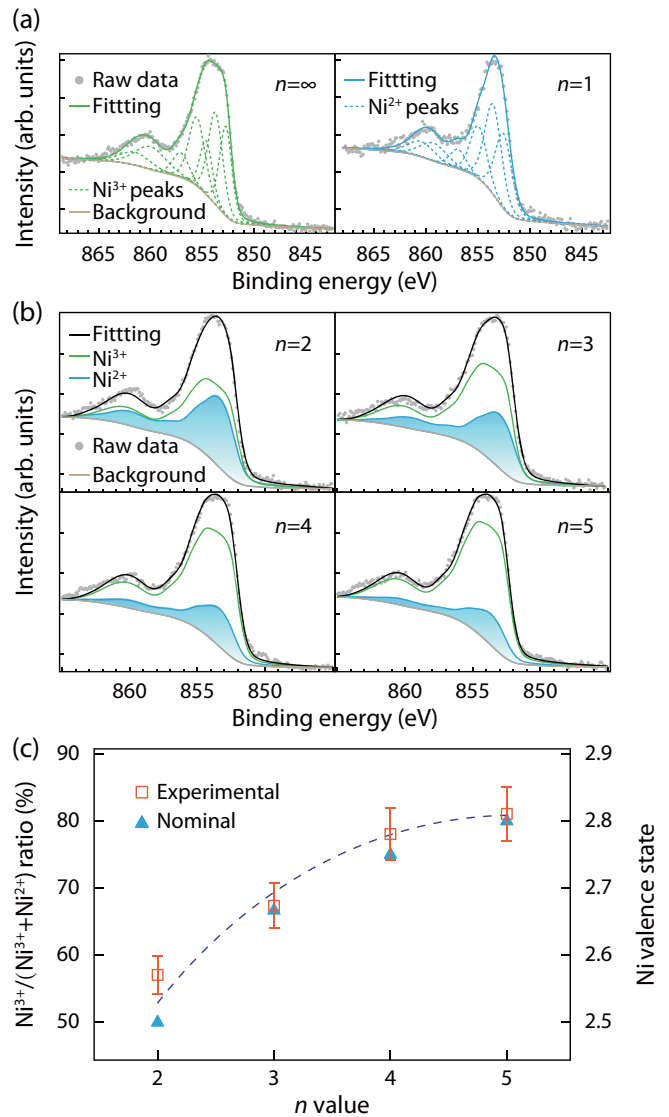

FIG. 3. (a) The Ni $2p_{3/2}$ spectra of NdNiO$_3$ and Nd$_2$NiO$_4$ fitted by multiplet splitting peaks using relative peak position, full width at half maximum, and area ratio suggested in Ref. [33]. (b) The Ni $2p_{3/2}$ spectra of $n = 2$–5 Ruddlesden-Popper (RP) films fitted using nonlinear least-squares fitting (NLLSF) method as mentioned in the main text. Gradient blue area represents the presence of Ni^{2+} species after spectra deconvolution. (c) The proportion of Ni^{3+} and corresponding Ni valence states in $n = 2$–5 RP films estimated from NLLSF analysis. Error bars represent uncertainty of the fitting process. Dashed line is the guide to the eyes.

substitutions. To verify this feature and quantify the evolution of Ni valence states, we performed XPS measurements, and the results are summarized in Fig. 3. It has been reported that multiplet splitting is necessary for verifying chemical states of Ni due to contributions from electronic coupling and screening effect [33]. Thus, we apply Ni^{3+} and Ni^{2+} multiplet envelopes from Ref. [33] to fit the Ni $2p_{3/2}$ spectra of NdNiO$_3$ and Nd$_2$NiO$_4$, respectively, using the XPST package [34]. The results are quite satisfying [Fig. 3(a)], indicating the expected dominant valence state of Ni being 3+ for NdNiO$_3$ and 2+ for Nd$_2$NiO$_4$. The core-level peak locates at ∼854.4 eV

for $NdNiO_3$ and 853.5 eV for Nd_2NiO_4, consistent with the results for $SmNiO_3$ (Ni^{3+}, 853.9 eV) [35] and NiO (Ni^{2+}, 853.4 eV) [36]. However, the fitting of intermediate valence (between Ni^{2+} and Ni^{3+}) spectra considering multiplet splitting would be much more complex for two sets of multiplet envelopes needed to be considered [33], which would complicate the refinement of fitting parameters and reduce the reproducibility of fitting results [37]. Thus, here, we use a nonlinear least-squares fitting (NLLSF) method [37] to deconvolute the Ni $2p_{3/2}$ spectra of other members ($n = 2$–5) using AVANTAGE software. The basic principle of NLLSF is to minimize the sum of squares of several nonlinear functions, here, the difference between the synthetic data envelope and the experimental spectra [38]. First, an initial guess (the reference spectra) is required before subsequent iterative optimization. Typically, the reference spectra can be obtained either from the standard data from a database or the derived data from peak fitting. In this paper, we assume that spectra changes of Ni $2p$ result from valence state variation of Ni. As such, the fitting curves of Ni $2p_{3/2}$ spectra of $NdNiO_3$ and Nd_2NiO_4 are used as references since they serve as the end members of the RP series with dominant Ni valence states of 3+ and 2+, respectively. During the fitting process, the maximum peak shift of each reference is set to 0.2 eV, and then the simulated envelope is automatically refined by successive iterations. Consequently, the fitting results only depend on the choice of reference spectra and the maximum peak shift [37]. Finally, the valence state of Ni is determined from the corresponding $Ni^{3+}/(Ni^{3+} + Ni^{2+})$ ratio, which is calculated from the area under each reference spectra by subtracting a Shirley-type background [Fig. 3(b)].

As shown in Fig. 3(c), the valence states of Ni show good agreement with nominal values, which were calculated from the chemical formula of each compound if considering Nd always being trivalent. Indeed, as shown in Fig. 4, the overall pattern of Nd $3d$ spectra is very similar for all RP members, where low binding energy satellites originating from the $3d$-$4f$ coupling can be clearly observed [39,40]. In addition, the main peak of Nd $3d_{5/2}$ locates at 982 ± 0.1 eV, in line with the values reported for $NdNiO_3$ thin films [39], indicating the trivalent nature of Nd cations in our films.

It is also known that the valence state of nickel is related to the formation of oxygen vacancy; however, the determination of its concentration from the fitting results of O $1s$ spectra (Fig. 5) is disturbed by the existence of different chemical bonds (ionic and covalent) and surface-related species. Specifically, the O $1s$ spectra can be deconvoluted into four peaks (peaks A–D) with detailed fitting parameters shown in Table I, suggesting the presence of different oxygen species in RP compounds [41–43]. It has been reported that the peaks $<\sim 531$ eV (peaks A and B in Fig. 5) correspond to the lattice O^{2-} anion [43], the origin of which can be ascribed to the coexistence of covalent and ionic bonds in perovskite nickelates [42,44]. On the other hand, peaks C and D mainly come from the metal hydroxides and weakly absorbed species (e.g., H_2O), respectively [42,43], and the former has been reported to relate to the oxygen vacancy concentration, considering the chemical activity of oxygen vacancy in metal oxides [44,45]. The amount of surface hydroxides estimated from the relative area of peak C is $\sim 30\%$ in our films, much lower than the
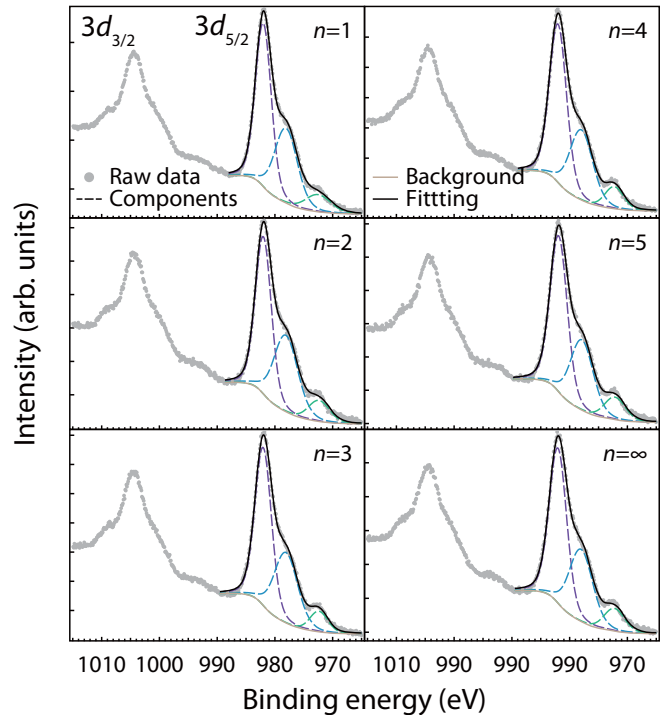

FIG. 4. The Nd $3d$ core-level spectra of Ruddlesden-Popper (RP) films, with the main peak position of Nd $3d_{5/2}$ spectra locating at ~ 982 eV across the RP series.
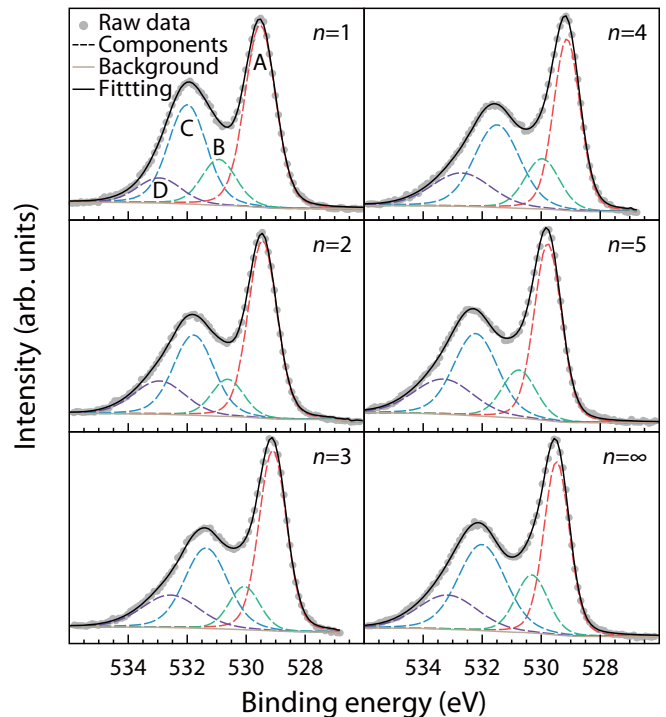

FIG. 5. The O $1s$ core-level spectra of Ruddlesden-Popper (RP) films. Following Ref. [42], four peaks (peaks A–D) with a Shirley-type background are included for the data fitting. The detailed fitting parameters are shown in Table I.

TABLE I. Fitting results of binding energy (BE), full width at half maximum (FWHM), and relative area (RA) for O $1s$ spectra of RP films. Peaks A–D are denoted in Fig. 5.

Sample	BE (eV)				FWHM (eV)				RA (%)			
	A	B	C	D	A	B	C	D	A	B	C	D
$n = 1$	529.53	530.93	531.99	532.95	1.23	1.38	1.53	1.76	46.40	13.12	31.41	9.07
$n = 2$	529.45	530.63	531.78	532.94	1.15	1.29	1.62	2.05	45.31	10.64	28.90	15.16
$n = 3$	529.09	530.01	531.36	532.71	1.09	1.20	1.83	2.20	42.33	10.52	34.03	13.12
$n = 4$	529.13	529.97	531.49	532.70	1.07	1.38	1.82	2.38	38.01	14.37	31.22	16.40
$n = 5$	529.78	530.75	532.22	533.31	1.09	1.36	1.76	2.39	39.70	13.43	29.71	17.16
$n = \infty$	529.48	530.32	532.01	533.17	1.02	1.29	1.90	2.40	35.65	14.99	32.92	16.44

value reported for LaNiO$_{3-\delta}$ powders ($\sim$68%) [44], indicating the much slighter oxygen-deficiency in our films.

In summary, RP structures can effectively adjust the d orbital occupancy of Ni, providing an opportunity to achieve similar electronic structure as high-T_c cuprates upon subsequent reduction.

C. Transport properties in RP neodymium nickelates

The temperature-dependent resistivities of RP films were measured using a standard collinear four-point probe method

[46], as shown in the inset of Fig. 6(a). Gold electrodes with equal spacing of 1 mm and thickness of 70 nm were deposited by ion sputtering to achieve ohmic contacts. As one of the most fascinating properties among perovskite rare-earth nickelates, MIT is considered most likely originating from the bond disproportionation [18,22]. In addition, it can be tuned by various manners, such as strain engineering [24], dimensionality control [26], and electrolyte gating [47]. As shown in Fig. 6(a), the NdNiO$_3$ film shows sharp MIT plus thermal hysteresis behavior, and the resistivity change reaches nearly
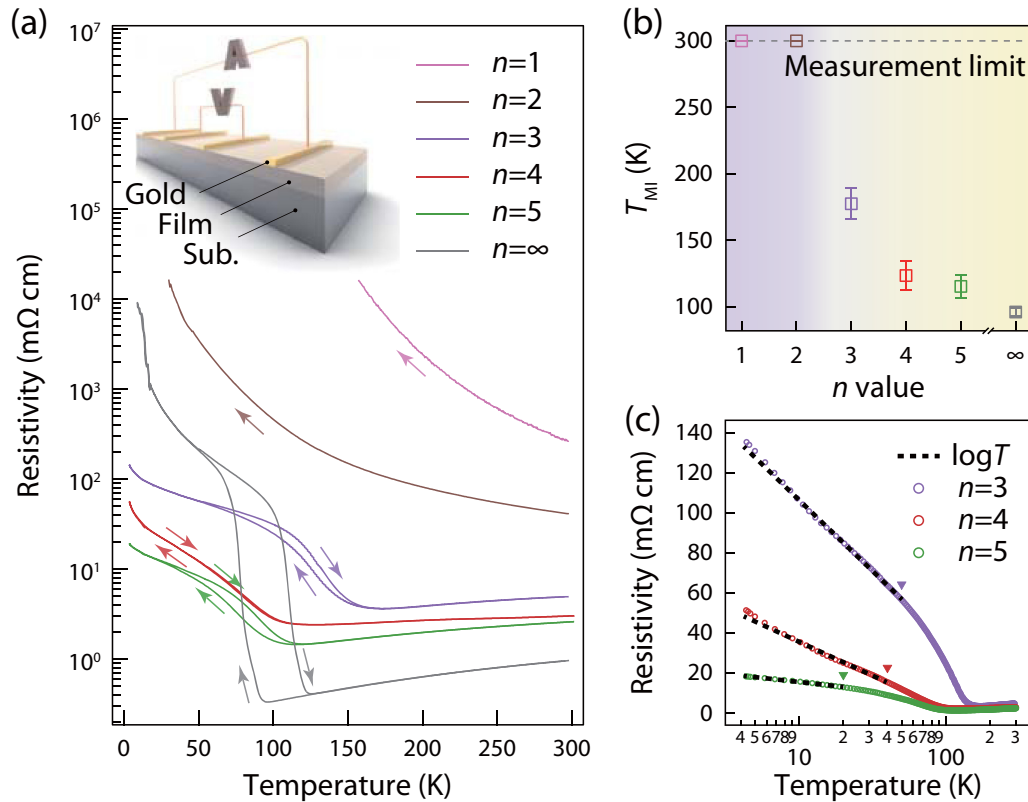

FIG. 6. (a) Temperature-dependent resistivities of $n = 1$–5 Ruddlesden-Popper (RP) films and a 22-u.c.-thick NdNiO$_3$ film. Arrows indicate the temperature-sweeping direction. The temperature-sweeping rate is kept at 2 K/min. Schematic of the collinear four-point probe geometry used for the transport measurements is shown in the inset. (b) T_{MI} of RP films during the cooling process. Error bars represent sample-to-sample variation. (c) Semilogarithmic plot of resistivities of $n = 3$–5 RP films during the cooling process. The black dashed lines are the corresponding log T fits. Triangles indicate the upper temperature limit for log T fits.

three orders of magnitude across MIT, in line with previous reports [47,48] and its single-crystalline PrNiO$_3$ counterpart [49,50]. This suggests the near optimal stoichiometry and high crystalline quality of the present NdNiO$_3$ film due to the fact that cation off-stoichiometry will dramatically change both the T_{MI} and the magnitude of resistivity change across the MIT [51,52]. Also, the influence of oxygen vacancy should be minimal, considering the comparable T_{MI} (~100 K) for NdNiO$_3$ grown on LAO substrates with similar thickness [47,53] since it is reported that oxygen vacancy tends to elevate the T_{MI} [53]. Furthermore, this in turn guarantees the right deposition time for each atomic layer of RP film growth, as they are determined from the codeposition process of NdNiO$_3$. For $n = 1$ and 2, insulating behavior is persistent in the whole temperature range (4–300 K), which most likely originates from charge ordering [4,54]. Interestingly, MIT and thermal hysteresis behavior appear for the members with $n \geqslant 3$, although with smaller resistivity change across MIT and weaker hysteresis than those of NdNiO$_3$. This is very similar to the case of some bulk RP nickelates, in which the hysteresis behavior is also very weak or even eliminated, perhaps manifesting the second-order or weakly first-order nature of this transition in RP phases with high n values ($3 \leqslant n < \infty$) [55–57].

Also, the T_{MI} exhibits clear n dependence, decreasing with increasing n value, which is clearly demonstrated in Fig. 6(b). This coincides with the thickness- and strain-dependent T_{MI} in NdNiO$_3$ films, where T_{MI} decreases as the Ni-O-Ni bond angle is straightened [53]. The straightened bond angle leads to larger orbital overlap between Ni 3d and O 2p; consequently, the electron hopping strength increases as does the stability of the metallic phase [18]. Here, in RP structures, the weakening of dimensionality effect with increasing n value [13] would also result in increasing orbital overlap between Ni 3d and O 2p; thus, higher electron hopping integral and lower T_{MI} are expected. This scenario is also compatible with the case in RNiO$_3$, where enhanced orbital overlaps between Ni 3d and O 2p from LuNiO$_3$ to LaNiO$_3$ lead to higher electron hopping strength. As a result, T_{MI} decreases from 600 K (in LuNiO$_3$) to 0 K (in LaNiO$_3$) [18]. In addition, the increasing of electron hopping strength would also be responsible for the decreasing of resistivity at the high-temperature metallic phase as n changes from 1 to ∞. Especially for the $n = 3$ member, both the MIT and metal-to-metal transition ~160 K have been documented for some polycrystalline counterparts [55–57], but the origins are still in controversy, which may be associated with the oxygen off-stoichiometry or phase purity [56]. In our case, all films were postannealed in 1.5 bar pure oxygen at 350 °C for 10 h before transport measurements to minimize the effect of oxygen vacancies, and the MIT behavior is robust within a series of $n \geqslant 3$ RP samples. Figure 6(c) shows the semilogarithmic resistivity curves of $n = 3$–5 RP films and log T fits of the corresponding semiconducting regime, which is defined as the temperature range between the lowest measured temperature and the beginning of the semiconducting transition [53]. In our case, the latter is ~50, 40, and 20 K for $n = 3$–5, respectively [marked by triangles in Fig. 6(c)]. Similar log T dependence has been observed in Nd$_4$Ni$_3$O$_{10-\delta}$ [57], infinite-layer nickelates (NdNiO$_2$) [58], and La$_{1-x}$Pr$_x$NiO$_{3-\delta}$ [59], where Ni-moment-centered Kondo
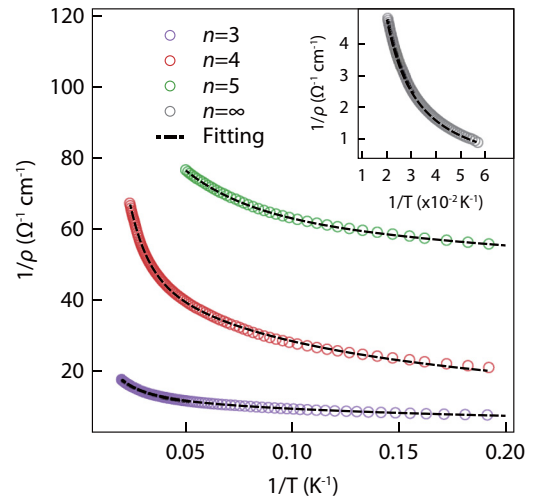

FIG. 7. Resistivity data fitting to the semiconducting state of $n = 3$–5 Ruddlesden-Popper (RP) compounds using the model combining thermally activated conduction and Mott variable range hopping, as proposed in Ref. [53]. Inset shows the fitting results for NdNiO$_3$.

scattering was proposed. However, the validity of the suggested Kondo-like scenario is still under debate in both RP and infinite-layer nickelates [56,60–62]. In addition, given the significant change of crystal and electronic structure after reduction, the presence of a Kondo-like scenario in reduced RP compounds (R_{n+1}Ni$_n$O$_{2n+2}$, $n = 3$–5) is an interesting open question to be explored in the future.

It is noted that the conductive behavior of the semiconducting state can be well described by a combination of thermally activated conduction and Mott variable range hopping (VRH) [53]. We performed the data fitting using Eq. (1) as reported in Ref. [53]:

$$\frac{1}{\rho} = A\exp\left(-\frac{B}{T^{1/4}}\right) + C\exp\left(-\frac{D}{T}\right), \quad (1)$$

where ρ is the resistivity, T is the temperature, and A, B, C, and D are constants. The fitting temperature range is 5–50, 5–40, 5–20, and 18–50 K for $n = 3$–5 and ∞, respectively. The resistivity data <18 K of NdNiO$_3$ ($n = \infty$) show lower signal-to-noise ratio, so 18 K was chosen as the lowest fitting temperature in this case. As shown in Fig. 7, the model with combined activated behavior and VRH can reproduce the experimental results well, suggesting the electron-phonon interaction and electron hopping both contribute to the conductivity. The activation energy extracted from the corresponding fitting is 8.4, 10.9, 2.9, and 16.8 meV for $n = 3$–5 and ∞ RP compounds, respectively. The deviation of activation energy for $n = 3$–5 RP compounds from the typical value for nickelates (~17–20 meV) [53] may be ascribed to the different degree of localized carriers and Ni^{2+} contents across the RP series, as suggested by the transport and XPS results.

IV. CONCLUSIONS

In conclusion, a series of Nd-based RP nickelates ($n = 1$–5) have been synthesized using MBE, especially the

metastable members with high n values. For $Nd_6Ni_5O_{16}$, both the square-planar crystal structure and $3d^{8.8}$ orbital occupation will be satisfied upon further topochemical reduction [6,15]. However, the exploration of reduction parameters is still challenging [63] and lies beyond the scope of this paper. Transport measurements demonstrate effective modulation of T_{MI} by changing the n value. Also, low-temperature resistivities of RP members with high n values show a clear log T dependence, like that of infinite-layer $NdNiO_2$, where Kondo scattering has been proposed as a possible underlying mechanism. Moreover, the valence states of Ni show good correspondence with the nominal values in the present RP series, as indicated by XPS results. Our work thus demonstrates the effectiveness of a layer-by-layer growth method

for stabilizing the metastable RP phases and provides another appealing platform for exploring high-T_c superconductivity and exotic properties in layered nickelates.

[1] S. N. Ruddlesden and P. Popper, Acta Crystallogr. **10**, 538 (1957).

[2] V. I. Anisimov, D. Bukhvalov, and T. M. Rice, Phys. Rev. B **59**, 7901 (1999).

[3] K. W. Lee and W. E. Pickett, Phys. Rev. B **70**, 165109 (2004).

[4] M. Uchida, K. Ishizaka, P. Hansmann, Y. Kaneko, Y. Ishida, X. Yang, R. Kumai, A. Toschi, Y. Onose, R. Arita, K. Held, O. K. Andersen, S. Shin, and Y. Tokura, Phys. Rev. Lett. **106**, 027001 (2011).

[5] H. Li, X. Zhou, T. Nummy, J. Zhang, V. Pardo, W. E. Pickett, J. F. Mitchell, and D. S. Dessau, Nat. Commun. **8**, 704 (2017).

[6] J. Zhang, A. S. Botana, J. W. Freeland, D. Phelan, H. Zheng, V. Pardo, M. R. Norman, and J. F. Mitchell, Nat. Phys. **13**, 864 (2017).

[7] D. Li, K. Lee, B. Y. Wang, M. Osada, S. Crossley, H. R. Lee, Y. Cui, Y. Hikita, and H. Y. Hwang, Nature (London) **572**, 624 (2019).

[8] D. Li, B. Y. Wang, K. Lee, S. P. Harvey, M. Osada, B. H. Goodge, L. F. Kourkoutis, and H. Y. Hwang, Phys. Rev. Lett. **125**, 027001 (2020).

[9] S. Zeng, C. S. Tang, C. Yin, C. Li, M. Li, Z. Huang, J. Hu, W. Liu, G. J. Omar, H. Jani, Z. S. Lim, K. Han, D. Wan, P. Yang, S. J. Pennycook, A. T. S. Wee, and A. Ariando, Phys. Rev. Lett. **125**, 147003 (2020).

[10] M. Osada, B. Y. Wang, B. H. Goodge, K. Lee, H. Yoon, K. Sakuma, D. Li, M. Miura, L. F. Kourkoutis, and H. Y. Hwang, Nano Lett. **20**, 5735 (2020).

[11] M. Osada, B. Y. Wang, B. H. Goodge, S. P. Harvey, K. Lee, D. Li, L. F. Kourkoutis, and H. Y. Hwang, Adv. Mater. **33**, 2104083 (2021).

[12] S. W. Zeng, C. J. Li, L. E. Chow, Y. Cao, Z. T. Zhang, C. S. Tang, X. M. Yin, Z. S. Lim, J. X. Hu, P. Yang, and A. Ariando, arXiv:2105.13492.

[13] Z. Li, W. Guo, T. T. Zhang, J. H. Song, T. Y. Gao, Z. B. Gu, and Y. F. Nie, APL Mater. **8**, 091112 (2020).

[14] J. Zhang and X. Tao, CrystEngComm **23**, 3249 (2021).

[15] M. R. Norman, Physics **13**, 85 (2020).

[16] E. M. Nica, J. Krishna, R. Yu, Q. Si, A. S. Botana, and O. Erten, Phys. Rev. B **102**, 020504(R) (2020).

[17] J. Q. Lin, P. Villar Arribi, G. Fabbris, A. S. Botana, D. Meyers, H. Miao, Y. Shen, D. G. Mazzone, J. Feng, S. G. Chiuzbăian, A. Nag, A. C. Walters, M. García-Fernández, K.-J. Zhou, J.

Pelliciari, I. Jarrige, J. W. Freeland, J. Zhang, J. F. Mitchell, V. Bisogni *et al.*, Phys. Rev. Lett. **126**, 087001 (2021).

[18] S. Catalano, M. Gibert, J. Fowlie, J. Íñiguez, J. M. Triscone, and J. Kreisel, Rep. Prog. Phys. **81**, 046501 (2018).

[19] R. S. Dhaka, T. Das, N. C. Plumb, Z. Ristic, W. Kong, C. E. Matt, N. Xu, K. Dolui, E. Razzoli, M. Medarde, L. Patthey, M. Shi, M. Radović, and J. Mesot, Phys. Rev. B **92**, 035127 (2015).

[20] E. Cappelli, W. O. Tromp, S. McKeown Walker, A. Tamai, M. Gibert, F. Baumberger, and F. Y. Bruno, APL Mater. **8**, 051102 (2020).

[21] A. Arab, X. Liu, O. Köksal, W. Yang, R. U. Chandrasena, S. Middey, M. Kareev, S. Kumar, M.-A. Husanu, Z. Yang, L. Gu, V. N. Strocov, T.-L. Lee, J. Minár, R. Pentcheva, J. Chakhalian, and A. X. Gray, Nano Lett. **19**, 8311 (2019).

[22] M. Imada, A. Fujimori, and Y. Tokura, Rev. Mod. Phys. **70**, 1039 (1998).

[23] G. Catalan, Phase Transit. **81**, 729 (2008).

[24] E. Mikheev, A. J. Hauser, B. Himmetoglu, N. E. Moreno, A. Janotti, C. G. Van de Walle, and S. Stemmer, Sci. Adv. **1**, e1500797 (2015).

[25] A. Biswas, C.-H. Yang, R. Ramesh, and Y. H. Jeong, Prog. Surf. Sci. **92**, 117 (2017).

[26] P. D. C. King, H. I. Wei, Y. F. Nie, M. Uchida, C. Adamo, S. Zhu, X. He, I. Božović, D. G. Schlom, and K. M. Shen, Nat. Nanotechnol. **9**, 443 (2014).

[27] Y. F. Nie, Y. Zhu, C. H. Lee, L. F. Kourkoutis, J. A. Mundy, J. Junquera, P. Ghosez, D. J. Baek, S. Sung, X. X. Xi, K. M. Shen, D. A. Muller, and D. G. Schlom, Nat. Commun. **5**, 4530 (2014).

[28] J. H. Lee, G. Luo, I. C. Tung, S. H. Chang, Z. Luo, M. Malshe, M. Gadre, A. Bhattacharya, S. M. Nakhmanson, J. A. Eastman, H. Hong, J. Jellinek, D. Morgan, D. D. Fong, and J. W. Freeland, Nat. Mater. **13**, 879 (2014).

[29] T. W. Zhang, Z. W. Mao, Z. B. Gu, Y. F. Nie, and X. Q. Pan, Appl. Phys. Lett. **111**, 011601 (2017).

[30] J. H. Haeni, C. D. Theis, D. G. Schlom, W. Tian, X. Q. Pan, H. Chang, I. Takeuchi, and X. D. Xiang, Appl. Phys. Lett. **78**, 3292 (2001).

[31] C.-H. Lee, N. J. Podraza, Y. Zhu, R. F. Berger, S. Shen, M. Sestak, R. W. Collins, L. F. Kourkoutis, J. A. Mundy, H. Wang, Q. Mao, X. Xi, L. J. Brillson, J. B. Neaton, D. A. Muller, and D. G. Schlom, Appl. Phys. Lett. **102**, 122901 (2013).

[32] P. L. Wise, I. M. Reaney, W. E. Lee, T. J. Price, D. M. Iddles, and D. S. Cannell, J. Eur. Ceram. Soc. **21**, 2629 (2001).

[33] A. P. Grosvenor, M. C. Biesinger, R. S. C. Smart, and N. S. McIntyre, Surf. Sci. **600**, 1771 (2006).

[34] M. Schmid, H.-P. Steinrück, and J. M. Gottfried, Surf. Interface Anal. **46**, 505 (2014).

[35] M. Kotiuga, Z. Zhang, J. Li, F. Rodolakis, H. Zhou, R. Sutarto, F. He, Q. Wang, Y. Sun, Y. Wang, N. A. Aghamiri, S. B. Hancock, L. P. Rokhinson, D. P. Landau, Y. Abate, J. W. Freeland, R. Comin, S. Ramanathan, and K. M. Rabe, Proc. Natl. Acad. Sci. USA **116**, 21992 (2019).

[36] H. Zhang, W. Wang, M. Chen, and H. Wan, Appl. Surf. Sci. **439**, 569 (2018).

[37] Z. Fu, J. Hu, W. Hu, S. Yang, and Y. Luo, Appl. Surf. Sci. **441**, 1048 (2018).

[38] G. Kemmer and S. Keller, Nat. Protoc. **5**, 267 (2010).

[39] K. Galicka, J. Szade, P. Ruello, P. Laffez, and A. Ratuszna, Appl. Surf. Sci. **255**, 4355 (2009).

[40] T. Onozuka, A. Chikamatsu, T. Katayama, Y. Hirose, I. Harayama, D. Sekiba, E. Ikenaga, M. Minohara, H. Kumigashira, and T. Hasegawa, ACS Appl. Mater. Interfaces **9**, 10882 (2017).

[41] L. Qiao and X. Bi, EPL **93**, 57002 (2011).

[42] S. Mickevičius, S. Grebinskij, V. Bondarenka, B. Vengalis, K. Šliužienė, B. A. Orlowski, V. Osinniy, and W. Drube, J. Alloys Compd. **423**, 107 (2006).

[43] J.-C. Dupin, D. Gonbeau, P. Vinatier, and A. Levasseur, Phys. Chem. Chem. Phys. **2**, 1319 (2000).

[44] W. Che, M. Wei, Z. Sang, Y. Ou, Y. Liu, and J. Liu, J. Alloys Compd. **731**, 381 (2018).

[45] H. P. Boehm, Discuss. Faraday Soc. **52**, 264 (1971).

[46] D. K. Schroder, *Semiconductor Material and Device Characterization* (Academic, New Jersey, 2005), Third ed., p. 9.

[47] R. Scherwitzl, P. Zubko, I. G. Lezama, S. Ono, A. F. Morpurgo, G. Catalan, and J.-M. Triscone, Adv. Mater. **22**, 5517 (2010).

[48] Q. Guo, S. Farokhipoor, C. Magén, F. Rivadulla, and B. Noheda, Nat. Commun. **11**, 2949 (2020).

[49] H. Zheng, J. Zhang, B. Wang, D. Phelan, M. J. Krogstad, Y. Ren, W. A. Phelan, O. Chmaissem, B. Poudel, and J. F. Mitchell, Crystals **9**, 324 (2019).

[50] T. Saito, M. Azuma, E. Nishibori, M. Takata, M. Sakata, N. Nakayama, T. Arima, T. Kimura, C. Urano, and M. Takano, Physica B: Condensed Matter **329-333**, 866 (2003).

[51] E. Breckenfeld, Z. Chen, A. R. Damodaran, and L. W. Martin, ACS Appl. Mater. Interfaces **6**, 22436 (2014).

[52] D. Preziosi, A. Sander, A. Barthélémy, and M. Bibes, AIP Adv. **7**, 015210 (2017).

[53] G. Catalan, R. M. Bowman, and J. M. Gregg, Phys. Rev. B **62**, 7892 (2000).

[54] M. Uchida, Y. Yamasaki, Y. Kaneko, K. Ishizaka, J. Okamoto, H. Nakao, Y. Murakami, and Y. Tokura, Phys. Rev. B **86**, 165126 (2012).

[55] Q. Li, C. He, X. Zhu, J. Si, X. Fan, and H.-H. Wen, Sci. China-Phys. Mech. Astron. **64**, 227411 (2020).

[56] D. Rout, S. R. Mudi, M. Hoffmann, S. Spachmann, R. Klingeler, and S. Singh, Phys. Rev. B **102**, 195144 (2020).

[57] B. Z. Li, C. Wang, P. T. Yang, J. P. Sun, Y. B. Liu, J. F. Wu, Z. Ren, J. G. Cheng, G. M. Zhang, and G. H. Cao, Phys. Rev. B **101**, 195142 (2020).

[58] G. M. Zhang, Y. F. Yang, and F. C. Zhang, Phys. Rev. B **101**, 020501(R) (2020).

[59] V. Hien-Hoang, N.-K. Chung, and H.-J. Kim, Sci. Rep. **11**, 5391 (2021).

[60] A. S. Botana, F. Bernardini, and A. Cano, J. Exp. Theor. Phys. **132**, 618 (2021).

[61] Y. Cui, C. Li, Q. Li, X. Y. Zhu, Z. Hu, Y.-F. Yang, J. S. Zhang, R. Yu, H.-H. Wen, and W. Q. Yu, Chin. Phys. Lett. **38**, 067401 (2021).

[62] Y. Xiang, Q. Li, Y. Y. Li, H. Yang, Y. F. Nie, and H.-H. Wen, Chin. Phys. Lett. **38**, 047401 (2021).

[63] K. Lee, B. H. Goodge, D. Li, M. Osada, B. Y. Wang, Y. Cui, L. F. Kourkoutis, and H. Y. Hwang, APL Mater. **8**, 041107 (2020).